Neuron, Vol. 47, 243–254, July 21, 2005, Copyright ©2005 by Elsevier Inc. DOI 10.1016/j.neuron.2005.06.004

Auditory Hair Cell-Afferent Fiber Synapses Are Specialized to Operate at Their Best Frequencies

M.E. Schnee,[1] D.M. Lawton,[2] D.N. Furness,[2] T.A. Benke,[3] and A.J. Ricci[1,*]

[1]Neuroscience Center and Kresge Hearing Labs
Louisiana State University
New Orleans, Louisiana 70112

[2]MacKay Institute of Communication and Neuroscience
Keele University
Keele
United Kingdom

[3]Departments of Pediatrics, Neurology, and Pharmacology
University of Colorado Health Sciences Center
Denver, Colorado 80262

Summary

Auditory afferent fiber activity is driven by high-fidelity information transfer from the sensory hair cell. Presynaptic specializations, posited to maintain fidelity, are investigated at synapses with characteristic frequencies of 120 Hz and 320 Hz. Morphological data indicate that high-frequency cells have more synapses and higher vesicle density near dense bodies (DBs). Tracking vesicular release via capacitance changes identified three overlapping kinetic components of release corresponding to morphologically identified vesicle pools. High-frequency cells released faster; however, when normalized to release site number, low-frequency cells released faster, likely due to a greater Ca^{2+} load per synapse. The Ca^{2+}-dependence of release was nonsaturating and independent of frequency, suggesting that release, not refilling, was rate limiting. A model of release derived from vesicle equilibration between morphologically defined pools reproduced the capacitance data, supporting a critical role in vesicle trafficking for DBs. The model suggests that presynaptic specializations enable synapses to operate most efficiently at their characteristic frequencies.

Introduction

Inner ear hair cells are specialized to maintain a high level of tonic synaptic release and to respond with graded release to varying stimulus amplitudes across a wide frequency range (Furukawa et al., 1978). Hair cell transmitter release drives afferent firing, transferring information about amplitude, frequency, and phase of stimulation (Crawford and Fettiplace, 1980). Although much is known about hair cell tuning mechanisms (Fettiplace and Fuchs, 1999), less is known about mechanisms responsible for maintaining high-fidelity transmission across this frequency range.

As in retinal cells, hair cells contain synaptic specializations, electron-dense ribbons or dense bodies (DBs), postulated to be involved in vesicle trafficking (Lagnado, 2003; Moser and Beutner, 2000; von Gersdorff and Matthews, 1999). Vesicles tethered to the DB are thought to comprise a readily releasable pool (rrp) (Gomis et al., 1999; Gray and Pease, 1971), while a subpopulation between the DB and the plasma membrane is thought to comprise the rapidly releasable pool, on the basis of kinetic measurements of release properties (Mennerick and Matthews, 1996; Moser and Beutner, 2000). The DB is proposed to maintain vesicles in the rrp for transfer to the rapidly released pool so that high release rates can be achieved (Eisen et al., 2004; Parsons et al., 1994; von Gersdorff and Matthews, 1999).

Cells containing synaptic ribbons or DBs have several common features implicating them in vesicle trafficking. First, they exhibit a high probability of release (Furukawa et al., 1978). Second, release can be maintained for seconds without depletion (Holt et al., 2004; Lagnado et al., 1996; Moser and Beutner, 2000; Parsons et al., 1994; Thoreson et al., 2004; von Gersdorff and Matthews, 1997). Third, multiple release rates have been reported that correlate with vesicle numbers in various pools (Moser and Beutner, 2000; Neves and Lagnado, 1999; von Gersdorff and Matthews, 1997). Finally, high rates of initial release have been measured (Lagnado et al., 1996; Neves and Lagnado, 1999; Rouze and Schwartz, 1998; von Gersdorff and Matthews, 1994; von Gersdorff et al., 1996).

The correlation of release rates with morphological assessment of hair cell synapses or the comparison of release rates between hair cells of different characteristic frequencies has not been previously reported and is the focus of these investigations. The major differences in synaptic properties between high- and low-frequency cells were in the number of synapses, the density of vesicles near the DB, and perhaps in the Ca^{2+} load per synapse, but not the Ca^{2+}-dependence of release. These differences are predicted to result in transmission being optimized to stimulus frequency. Three phases of release were identified, however, with little saturation between components due to considerable temporal overlap. This suggests that DBs facilitate vesicle trafficking such that release, not refilling, is rate-limiting, except for the initial 20 ms of stimulus. This initial disparity appears to account for the adaptive run-down observed by Furukawa and Matsuura (Furukawa and Matsuura, 1978).

Results

Hair cells from two papilla locations, measured as the relative distance from the apical end ($d = 0.3 \pm 0.05$, $n = 37$ and $d = 0.59 \pm 0.03$, $n = 67$) and corresponding to characteristic frequencies of 120 ± 15 Hz and 320 ± 5 Hz were investigated. To determine the number of fibers innervating a given hair cell at each position, the cut end of eighth nerve fibers were loaded with Alexa 488 dye crystals. Figures 1A and 1B show representative two-photon optical sections through afferent fibers

*Correspondence: aricci@lsuhsc.edu

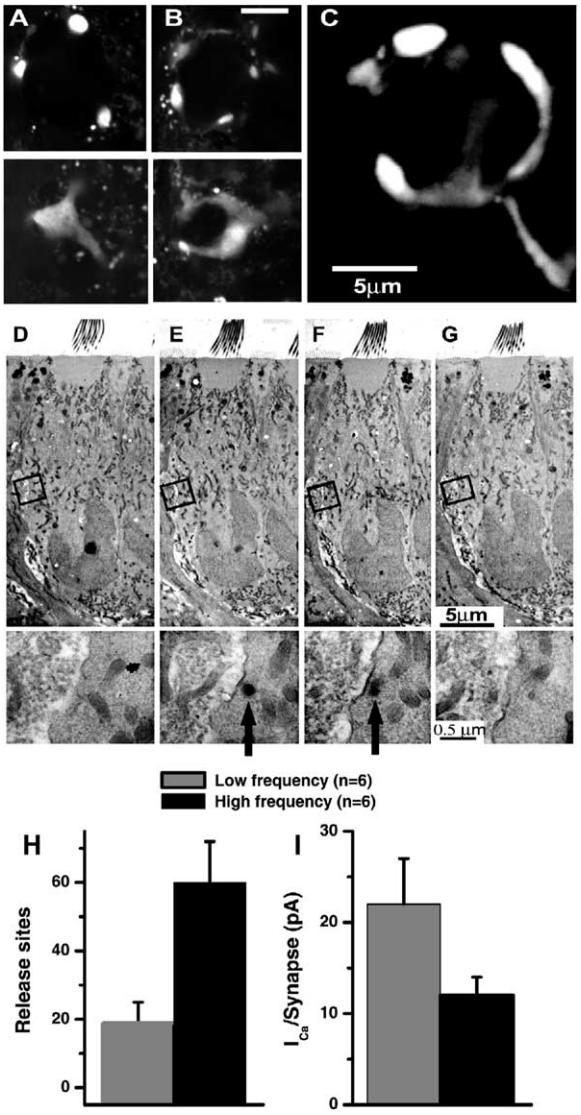

Figure 1. Comparison of Innervation Patterns between Frequency Locations

(A–C). Two-photon imaging of Alexa 488-loaded primary afferent terminals from low-frequency (A) and high-frequency fibers (B). Upper panels, optically sectioned near the top of the fibers, show a number of finger-like projections, while the lower panel shows a basal section of the hair cell, demonstrating that projections converge onto a single afferent fiber. The small fluorescent dots could not be traced to fibers, but may represent efferent terminals also filled with dye. (C) A z-stack reconstruction of 27 serial optical sections captured with the two-photon system illustrates a single fiber innervating a hair cell. Scale bars, 5 μm. (D–G) Transmission electron micrograph of four semithin serial sections (300 nm) from a low-frequency hair cell, illustrating the technique used for identifying and locating dense bodies. Boxes indicate the region shown at higher magnification below. A DB is observed in the two middle sections in this expanded view (below). Identification of DBs was performed at the higher magnification. Scale bars in upper panels, 5 μm; scale bars in lower panels, 0.5 μm. (H) Bar graph showing the number of dense bodies per hair cell from high- and low-frequency position. (I) Bar graph of maximum I_{Ca} per synapse. Error bars in (H) and (I) represent the mean ± SD.

innervating high- (n = 14) and low-frequency (n = 17) hair cells. The upper optical sections were taken near the tips of the fibers, about halfway up the hair cell, showing the finger-like terminal projections, while those below, near the base of the hair cell, illustrate each process converging onto one fiber. A Z-stack (vertical montage) of all image planes through a single terminal field and fiber is shown in Figure 1C, where the finger-like afferent terminals converge near the cell's base to form a single fiber. The number of finger-like projections for each hair cell increased slightly from 3 ± 0.2 (n = 17) to 4 ± 0.2 (n = 14) for low- and high-frequency positions, respectively, similar to electron microscopic reconstructions (Sneary, 1988). Each fiber was traced to the neural edge of the papilla; no branching was observed over this distance, indicating that one fiber innervates one hair cell, thus allowing presynaptic data to be interpreted in terms of synaptic release onto a single nerve fiber.

Serial semithin sections were evaluated by transmission electron microscopy (TEM) to determine the number of synapses per hair cell. Synapses were defined by the presence of a dense body (DB) opposed to synaptic thickenings. DBs not associated with thickenings were excluded. There were no synaptic thickenings identified that did not lie adjacent to a DB, and no DB was associated with more than one synaptic thickening. A series of four 300 nm sections from an apical hair cell is presented in Figures 1D–1G. The boxes indicate the expanded region just below each section. Profiles of a single DB are observed in the two middle panels, but not in the first or last panel. Low-frequency cells had 18 ± 7 (n = 6) synapses, while high frequency cells had 60 ± 12 (n = 6) synapses (Figure 1H), values similar to those found by Sneary (Sneary, 1988).

Previous work has shown that the hair cell Ca^{2+} current (I_{Ca}) is carried by L-type (α1D-type) channels (Kollmar et al., 1997; Schnee and Ricci, 2003) that cluster near synaptic release sites, so that all measured current can be ascribed to release sites (Issa and Hudspeth, 1994; Ricci et al., 2000; Roberts et al., 1990; Tucker and Fettiplace, 1995; Zenisek et al., 2003). Maximal I_{Ca} amplitudes were 400 ± 98 pA (n = 33) and 687 ± 131 pA (n = 67) for low- and high-frequency cells, respectively. Assuming that all release sites are functional, each site has 22 ± 5 pA and 12 ± 2 pA of I_{Ca} maximally for low- and high-frequency positions (Figure 1I). Thus, despite low-frequency cells having smaller maximal currents in comparison to those of high-frequency cells, they appear to have more I_{Ca} per release site.

As synaptic morphology provides the framework for understanding synaptic transmission, a quantitative assessment of synaptic architecture was performed. Serial ultrathin (40 nm) sections of DBs and surrounding regions were examined at 100,000×using TEM (Figure 2). Ten low-frequency DBs and 11 high-frequency DBs were completely reconstructed. Only one DB was reconstructed per cell. The morphologically defined vesicle pools are defined in Figure 2B. Examples of single sections through DBs from a low-frequency and a high-frequency cell are shown in Figure 2C to illustrate the similarity in structures. No difference in synaptic thickening length, 598 ± 88 nm for low- and 522 ± 78 nm for

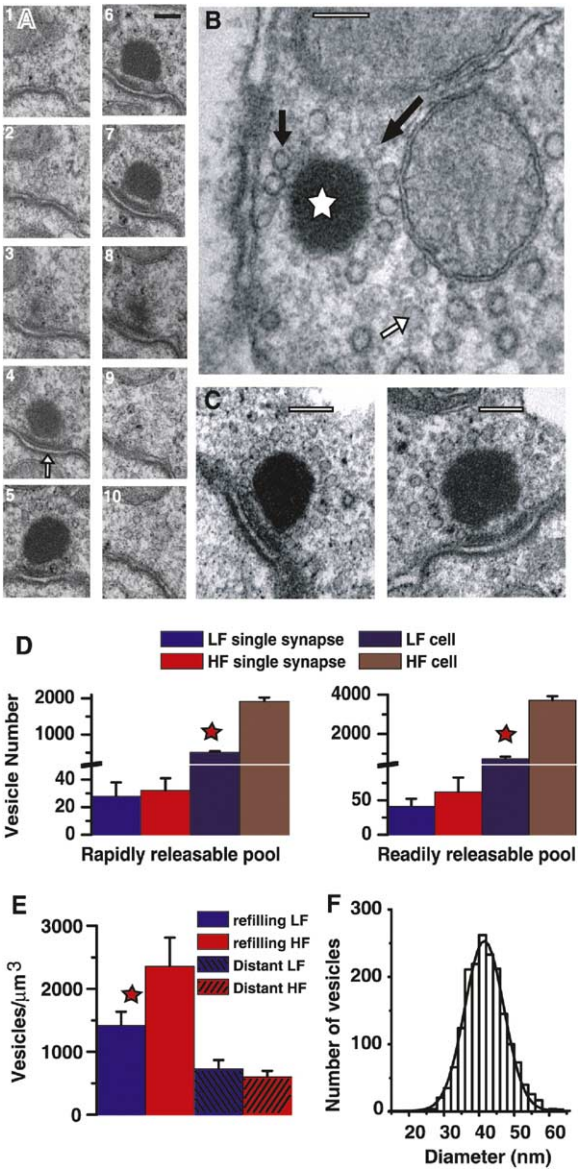

Figure 2. Serial Reconstruction of Thin 40 nm Section TEM Images of DBs Allows Quantification of Synaptic Structures

(A) Example of serially sectioned DB. Numbers represent order of sections. White arrow (panel 4) indicates synaptic thickening. (B) Example of a single section through the center of a DB (white star). Short black arrow indicates vesicle in rapidly releasable pool; long black arrow indicates vesicle in readily releasable pool; and white arrow indicates vesicle in refilling pool. (C) Single section examples of DB from low-frequency (left) and high-frequency (right) cells. (A)–(C): Scale bar, 200 nm. (D) Bar graphs comparing vesicle populations per synapse (red and blue) and per cell (navy and brown) for high- and low-frequency cells for both the rapidly and readily releasable pools. Red star indicates significance from the corresponding frequency position at $p < 0.001$. (E) Comparison of vesicle density for refilling and distant pools for high- and low-frequency cells. Red star, $p < 0.001$. Error bars, in (D) and (E) represent the mean ± SD. (F) Frequency histogram of vesicle diameter. Vesicles from high- and low-frequency cells were pooled. Population includes a total of 1834 DB-associated vesicles: 1070 from high- and 764 from low-frequency DBs. The fit to a normal distribution centered at 42 nm with a half-width of 11 nm and $r^2 = 0.99$.

high-frequency synapses, was found. There was a slight increase in DB diameter, relative to the characteristic frequency of the hair cell, ranging from 218 ± 19 nm (n = 10, low-frequency) to 252 ± 33 nm (n = 11, high-frequency, $p < 0.05$), not nearly as dramatic as that described in chick, where DB diameters varied from 120 to 250 nm (Martinez-Dunst et al., 1997), albeit over a larger frequency range. DBs were smaller than those in vestibular organs of frog and goldfish saccule, where their diameters were ~400 nm (Gleisner et al., 1973; Hama and Saito, 1977; Jacobs and Hudspeth, 1990; Lenzi et al., 1999).

The number of vesicles per DB was 69 ± 11 (n = 7) and 94 ± 21 (n = 11) for DBs obtained from low- and high-frequency cells, respectively. The difference in number between frequency locations, ($p < 0.05$) could be explained by the difference reported for DB diameter. Vesicle numbers per DB represent 53% and 51% of maximal density, proportions similar to those for saccule hair cell DBs (Lenzi et al., 1999).

The population of vesicles on the DB was subdivided into two pools, those between the plasma membrane and DB (rapidly releasable pool) and those on the DB, but away from the plasma membrane (readily releasable pool) (Figure 2D). The number of vesicles in the rapidly releasable pool were similar (28 ± 10, n = 10 and 32 ± 9, n = 11) for low- and high-frequency positions, respectively. The number of vesicles in the readily releasable pool is equivalent to the difference between the total number of vesicles on the ribbon and that in the rapidly releasable pool. As illustrated in Figure 2D, although the differences between synapses were not great, the greater number of synapses in high-frequency cells results in their having significantly more vesicles in each of these pools.

Reconstructions of saccule hair cell DBs revealed a gradient in the cytosolic synaptic vesicles, where vesicle numbers decrease with distance away from the DB (Lenzi et al., 2002; Lenzi et al., 1999). Vesicle concentrations were measured at two positions relative to the DB, vesicles within a ~700 nm radius from the center of the DB (near), and those greater than ~1 μm away from the DB and extending toward the center of the cell (distant). Vesicles near the DB were counted in serial sections. Volumes were calculated using 40 nm as the section thickness and subtracting mitochondrial and DB volumes. Vesicle concentrations were 1416 ± 220 vesicles/μm^3 (n = 7) and 2354 ± 459 vesicles/μm^3 (n = 11) for low- and high-frequency cells (statistically different, $p < 0.001$), respectively (Figure 2E). For measurements of the distant pool, single 40 nm sections were used at a magnification of 36,000×. Here too, mitochondrial volumes were subtracted. Concentrations of 595 ± 132 vesicles/μm^3 (n = 8) and 475 ± 98 vesicles/μm^3 (n = 11) for low- and high-frequency cells were obtained; these values were not statistically different ($p > 0.05$) from each other, but were statistically different ($p < 0.001$) from those for the near pool. Thus, vesicles are concentrated near DBs and release sites, and the vesicle density is greater near high- frequency DBs than low-frequency DBs. Values indicate that a hair cell can have more than 1,000,000 vesicles throughout its cell body, a value similar to that reported

for retinal bipolar neurons (Lagnado et al., 1996; von Gersdorff et al., 1996).

Vesicular release may come from multiple sources, the DB providing one route of exocytosis, while more traditional vesicle docking at the plasma membrane may also occur. To determine if non-DB-associated release might contribute to the total release, docked vesicles were counted along the membrane for distances up to 1 μm away from the DB. As no difference was noted between frequency locations, data were pooled with the resultant value of 0.5 ± 1.0 vesicles/μm (n = 20) comparable, though smaller than, that reported for the saccule (Lenzi et al., 1999). Thus, vesicular release is interpreted and modeled as being trafficked via the DB.

Vesicle diameters were measured from vesicles within 30 nm of the DB by determining the area of the vesicle and calculating the diameter of a circle of equivalent area (Lenzi et al., 1999; Usukura and Yamada, 1987). Frequency histograms of vesicle diameters, generated for populations obtained from low- and high-frequency DBs, were fit with a single normal distribution. No difference was found between populations; therefore data were pooled (presented in Figure 2F). A normal distribution with a mean of 42 ± 6 nm (n = 1834) was obtained, similar to the 45 nm reported for goldfish saccule (Hama and Saito, 1977), but slightly larger than the mean distribution obtained from frog saccule DBs (34 nm) (Lenzi et al., 1999), frog crista ampullaris (35 nm) (Gleisner et al., 1973), or retinal bipolar vesicles (29 nm) (von Gersdorff et al., 1996). To assess whether section thickness altered measured values, sections of 50, 70, and 90 nm were obtained, and vesicle diameters were compared (von Gersdorff et al., 1996). Values of 42 ± 5 (n = 35), 42 ± 3 (n = 20), and 43 ± 4 (n = 20), respectively, were measured, demonstrating that section thickness did not bias the measurements. Assuming a specific capacitance of 1 $\mu F/cm^2$ and a spherical shape for the vesicles gives a capacitance of 50 aF per vesicle.

The ultrastructural framework of DBs and synapses in high- and low-frequency cells was used to assist in the design of the physiological measurements and to derive models of vesicular release.

The sine wave stimulus used to measure capacitance (stopped briefly to elicit I_{Ca}), the I_{Ca}, the resulting capacitance changes, and the resistance changes are all shown in Figures 3A and 3B. Only experiments in which resistance was constant were included. Blocking I_{Ca} with external application of 1 mM cadmium eliminated the capacitance change (Figure 3A), supporting the conclusion that the changes measured reflect Ca^{2+}-dependent exocytosis. To further investigate the Ca^{2+} dependence, the magnitude of capacitance change was measured at membrane potentials activating different amplitudes of I_{Ca} (Figure 3B). Larger I_{Ca} elicited larger capacitance changes. Superposition of normalized steady-state I_{Ca} and normalized capacitance change plotted against membrane potential (Figure 3C) indicate that the capacitance change was linked to Ca^{2+} entry.

Endocytosis was recorded in most cells. The time course of capacitance reduction was recorded for stimulus durations between 300 ms and 10 s and fit with an exponential equation. As no difference was found for stimuli of different durations, data were pooled, giving a time constant of 7 ± 2 s (n = 12), demonstrating that

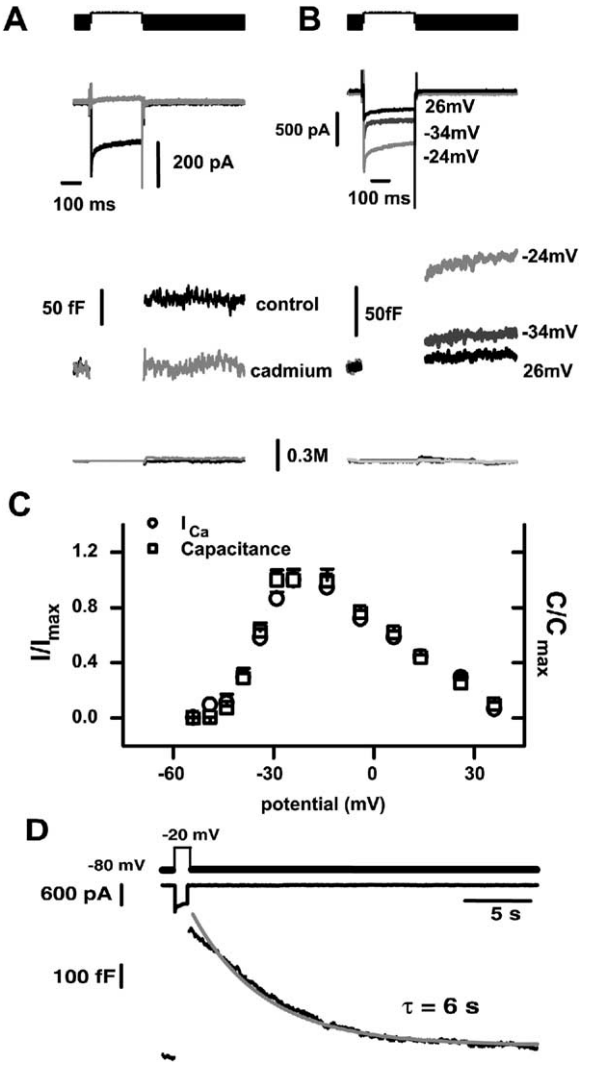

Figure 3. Ca^{2+} Entry Drives Membrane Capacitance Changes

(A) Example of a capacitance change elicited by a 300 ms depolarization to –24 mV. Top trace shows the stimulus, in which the thick line represents a sine wave that is blanked during the depolarizing step; I_{Ca} is seen in the second panel down; capacitance traces, in the third panel down, with the blank region representing a depolarizing step; and the bottom traces demonstrate resistance. Black lines indicate the control, and gray lines, the measurements in the presence of 1 mM of the Ca^{2+} channel blocker Cd. Cd blocked both the I_{Ca} and the capacitance increase (99% block; n = 4). No resistance changes were observed in any of the data presented.

(B) Panels show the same components as those in (A), and here the voltage step was varied to elicit different magnitudes of I_{Ca}.

(C) Summary of data collected in (B); circles represent the normalized steady-state I_{Ca} and squares, the normalized capacitance data plotted against the membrane potential of the step depolarization. Normalization was to the maximal value at –24 mV.

(D) Example of the time course of endocytosis in response to a 1 s depolarization. Upper panel is the stimulus, middle panel is the I_{Ca}, and the lower panel is capacitance. The time constant was 6 s (gray line).

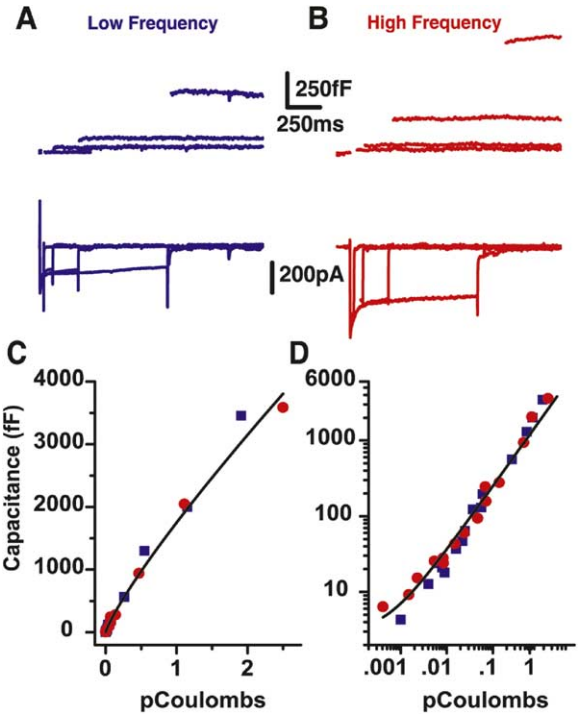

Figure 4. High- and Low-Frequency Cells Have the Same Ca^{2+} Dependence of Release

(A and B) Upper panels show capacitance response and lower panels, the I_{Ca} for a low-frequency (A) and a high-frequency cell (B) in response to increasing durations of depolarization. Depolarizations were to –24 mV; durations shown are 10, 100, 250, and 1000 ms.

(C) Integrating I_{Ca} allowed for the normalization of the current amplitude between the two frequency locations. Plotting the integral of I_{Ca} against capacitance change reveals a power plot with a power of 0.90 ± 0.03fF/pC (r^2 = 0.99). No difference was observed between high-frequency (red circles) and low-frequency (blue squares) positions. Error bars, representing SD, were smaller than the symbol sizes. The number of cells for each data point varied between 4 and 56 for high-frequency cells and 3 and 31 for low-frequency cells.

(D) Replotting the data from (C) on a log-log plot better reveals all of the data points used to generate this plot.

only long-duration capacitance measurements (>3s) will be underestimated due to endocytosis.

The Ca^{2+} dependence and rates of release were evaluated from capacitance changes in response to increasing durations of depolarization (Figures 4A and 4B). High-frequency cells (Figure 4B) had larger I_{Ca} and larger capacitance changes than low-frequency cells (Figure 4A). Long-duration pulses elicited large nonsaturating changes in capacitance qualitatively similar to those reported in other hair cells (Eisen et al., 2004; Moser and Beutner, 2000; Parsons et al., 1994). To normalize for both the difference in I_{Ca} amplitudes between frequency locations and for inactivation of the I_{Ca}, capacitance was plotted against the integral of the current (Figure 4C). The plot, fit by a power function with a power of 0.90 ± 0.03, was similar to that of mature inner hair cells (Johnson et al., 2005). No difference was observed in the Ca^{2+} dependence of release between high- and low-frequency hair cells. To better resolve the range of data points included, a log-log plot is shown in Figure 4D. The large range of capacitance values over which the slope remained constant is surprising because multiple vesicle recruitment steps are required to account for all needed vesicles—steps that might be predicted to alter Ca^{2+} dependence. For an average high-frequency hair cell, if all the vesicles on all of the DBs were released (60 DBs × 94 vesicles/DB = 5640), a capacitance change of 282 fF (5640 × 50 aF) is anticipated. Thus, capacitance values less than this indicate that only vesicles on the DB were used. The capacitance change of 3.6 pF for a 10 s stimulation equates to 72,000 vesicles, requiring vesicles from the surrounding pool to refill each DB ~13x (72,000/5640) in 10 s. Similarly, for an average low-frequency cell, all of the vesicles on the DBs (18 DBs × 69 vesicles/DB = 1242 vesicles) could account for a capacitance change of 62 fF; thus, the capacitance change at 10 s (2.0 pF) requires each DB to refill 32 times in 10 s. Yet, despite the differences in vesicle pools and the refilling required to account for the different capacitance values, the Ca^{2+} dependence remained constant, suggesting that refilling was not rate limiting.

The kinetics of release was investigated by plotting capacitance data from Figure 4 against pulse duration (Figure 5). Three plots, each with a different timescale, are presented to illustrate the different kinetic components. In Figure 5A, the analysis is limited to a duration that includes only points fit with a single exponential equation. For low-frequency cells this was 75 ms and the 100 ms point shown was not included in the fit, while for high-frequency cells, this included the 100 ms point, but not the 200 ms point (value was 240 fF at 200 ms). The solid vertical bars in the figure represent the predicted range of capacitance values (min/max) estimated from morphological data by using the product of the number of synapses and the number of vesicles in the rapidly releasable pool. In each case, the asymptote of the fit was within this morphological boundary and the capacitance value excluded was outside this predicted range. The time constants for depletion of this fast pool were 46 ± 3 ms and 18 ± 3 ms for high- and low-frequency responses, respectively, suggesting that low-frequency cells deplete this pool more quickly than do high-frequency cells; this hypothesis is supported by the morphological data demonstrating that there are fewer rapidly releasable vesicles in low-frequency cells (Figure 2D).

Figure 5B similarly shows capacitance values plotted against stimulus durations up to 300 ms; again, a duration was selected by increasing the points included until the exponential fit no longer represented the data. Here the data were fit with double exponentials where the first component is equivalent to the fits for Figure 5A and the second represents recruitment of a second pool of vesicles. Morphologically this pool is presumed to be the vesicles remaining on the DB (readily releasable pool) and is represented by the vertical bars on the right-hand side of the plot. The fit to the data is close to the morphological estimates.

The plot in Figure 5C represents all tested time points and is predominated by longer depolarizations eliciting large capacitance changes. The solid lines are fits from a mass action model described below. The data indi-

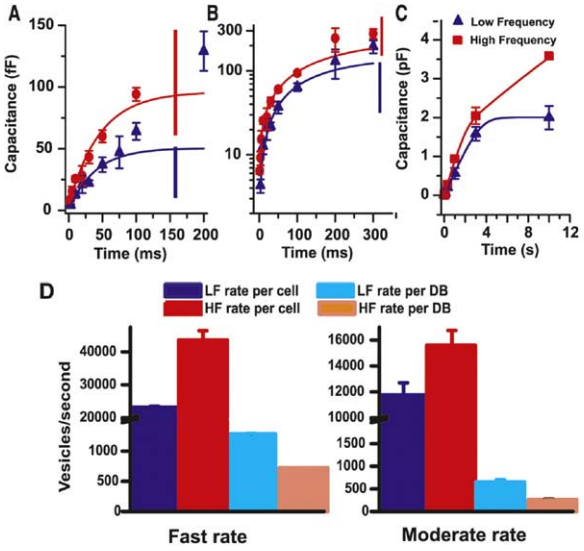

Figure 5. Three Kinetic Components of Release Correlate with Morphologically Defined Vesicle Pools

(A) Plotting capacitance change against stimuli up to 100 ms shows a fast release that plateaus near the predicted values for vesicles between the DB and plasma membrane (indicated by bars). Exponential fits (solid lines) had time constants of 18 ± 6 ms and 46 ± 3 ms, with plateau values of 50 ± 10 fF and 91 ± 15 fF for low- and high-frequency cells, respectively. (B) Extending the plot out to 300 ms revealed a second, slower release rate. Data were fit with double-exponential (solid lines), using values from the fit from (A) for the fast component. Time constants of 175 ± 60 ms and 233 ± 50 ms with plateaus of 148 ± 31 fF and 155 ± 22 fF were obtained for low- and high-frequency data, respectively. The solid bars represent the morphological prediction of capacitance to include all the vesicles on the DB. (C) Plots of capacitance change against stimulus durations out to 10 s. A third component of release was observed. Data here are fit to a mass action model explained in the text and Figure 7 and the fitting parameters given in Table 1. Error bars in (A)–(C) represent the mean ± SD. (D) Release rates taken from the steepest portion of the plots in (A) for the fast rate and from the steep portion of the second component of release in (B) for the moderate rate. Rates are given per cell or normalized to the number of release sites. In both cases the rates for the high- and low-frequency cells are statistically different at the $p < 0.01$ level. Error bars in (D) and (E) represent the mean ± SEM.

cate that release from low-frequency cells is depleted after approximately 2 s, but in high- frequency cells release can be maintained for durations greater than 10 s.

Release rates were estimated from the steepest slope of each release component in Figures 5A and 5B for the rapidly and readily releasable pools (Figure 5D). High-frequency cells released at significantly faster rates than low-frequency cells from both pools ($p < 0.001$), reaching rates as fast as those reported for bipolar cell synaptic ribbons (Mennerick and Matthews, 1996). When normalized to release per synapse, however, low-frequency synapses operated at higher rates than the high-frequency synapses ($p < 0.001$). This may be related to the higher Ca^{2+} entry per synapse (Figure 1I) in low-frequency cells and may underlie their faster depletion compared with that in high-frequency cells.

Identification of multiple release rates corresponding to morphologically identified pools of vesicles is consistent with data from other ribbon synapses (Neves and Lagnado, 1999; von Gersdorff and Matthews, 1997) and with data from other hair cells (Moser and Beutner, 2000; Parsons et al., 1994; Johnson et al., 2005). However, the major differences are in the magnitude of release, likely a reflection of the number of synapses, and in the limited plateau observed between each phase of release. That is, the three kinetic components overlapped in time, limiting depletion of both the rapidly and readily releasable pool of vesicles. In contrast to other ribbon synapses, a clear plateau in release that corresponded to depletion of one pool prior to recruitment of the next pool was not observed.

The limited separation between kinetic components and the linear Ca^{2+} dependence of release led to the hypothesis that the rate-limiting step of transmission is vesicle fusion, and not pool replenishment. If refilling is rate limiting, then the Ca^{2+} dependency would not be linear over such a broad range of capacitance values and more of a plateau would be observed between phases of release. If release is faster than refilling, then multiple stimulations over brief periods of time would saturate release by depleting releasable pools of vesicles (Figure 6). Capacitance changes were measured in response to a series of rapid depolarizations of different durations and interpulse intervals (IPI). Stimulus durations were initially chosen to match capacitance values predicted to correlate with the rapidly or readily releasable pool of vesicles on the basis of the morphological measurements. Examples of capacitance and I_{Ca} responses are presented in Figure 6 for a low- and a high-frequency cell in response to 50 ms depolarizations to –24 mV every 100 ms. On average, capacitance changes of approximately 41 ± 11 fF (n = 4 cells) per step for the high-frequency cells and 24 ± 5 fF (n = 9 cells) for the low-frequency cells were obtained. No cell failed to respond to any of the ten sequential steps, despite eliciting capacitance changes equivalent to the DBs' turning over all of their vesicles 3.8 times for low- and 1.5 times for high-frequency cells, respectively. The maximal responses were comparable to a single 500 ms pulse. In most cells, shortening of the IPI did not result in reduction in capacitance, but instead led to potentiation of the capacitance response, likely due to lack of Ca^{2+} clearance between stimuli (data not shown). Here too, data indicate that synapses were capable of rapidly replenishing their release pools, implying that vesicle fusion, and not vesicle trafficking, may be rate limiting. To further investigate this possibility, sequential pulses of longer duration were tested. Figure 6B shows plots of capacitance and I_{Ca} responses to 1 s depolarizations with 100 ms IPI from both frequency locations. Both responses demonstrate some plateau in the capacitance response, with low- frequency cells reaching the plateau more rapidly than high-frequency cells. A normalized cumulative plot of capacitance against stimulus time illustrates the difference between high- and low-frequency cells. The mass action model described below accurately simulates the data (solid lines, Figure 6C). The maximal capacitance values obtained were 3.7 ± 0.5 pF (n = 5) and 1.9 ± 0.2 pF (n = 4) for high- and low-frequency cells, respectively, again comparable to the values obtained for a single 10 s pulse, and suggesting that the vesicles on the DBs are

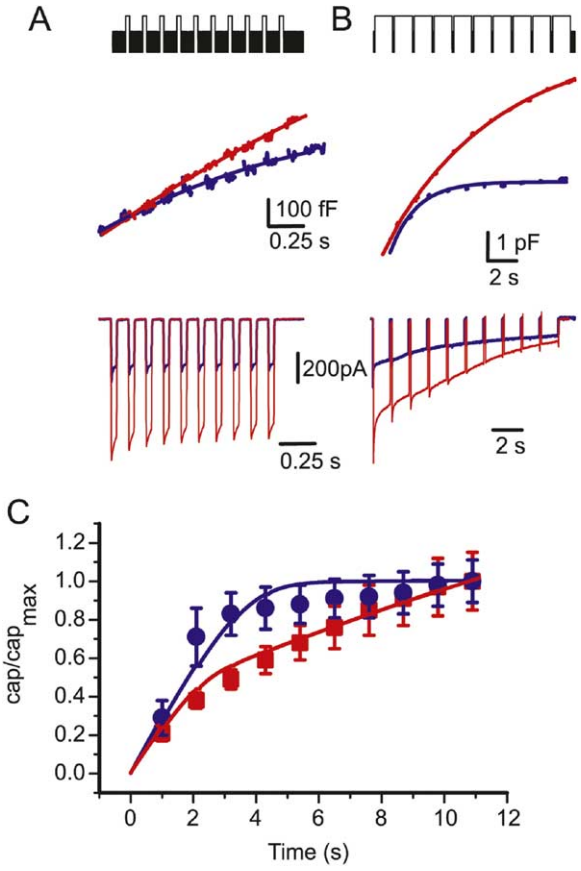

Figure 6. Multipulse Experiments Define Vesicle Pools

(A) Stimulus at the top, capacitance traces in the middle, and I_{Ca} at the bottom for high- (red) and low- (blue) frequency responses to a series of ten 50 ms duration pulses to –24 mV with 100 ms interpulse intervals. Neither cell showed saturation despite releasing vesicles accounting for more than the number of vesicles per DB.

(B) The data are ordered similarly to those in (A), but 1 s duration pulses with 100 ms interpulse intervals were used. Both cells show some saturation, with low-frequency cells saturating more completely and faster than the high-frequency cells.

(C) Summary of high-frequency (squares, n = 5) and low-frequency (circles, n = 4) capacitance responses to the protocol in (B) (normalized to maximal response). Solid lines represent the mass action model simulation of the data. Error bars represent the mean ± SD.

turning over 13 and 31 times, respectively. The maximal capacitance changes elicited at the end of sequential pulses amounted to 38,000 and 74,000 vesicles for low- and high-frequency cells, which requires vesicles within 1.05 μm and 0.35 μm of the DB for low-frequency cells and high-frequency cells, respectively, to be recruited and released. This difference might explain why release from low-frequency cells plateaus, whereas that from high-frequency cells does not. This result indicates that DBs can be rapidly replenished from the surrounding population of vesicles and suggests that the density of vesicles in this region is critical for determining how long the synapse can operate. Simulations with the model described below, i.e., the solid lines in Figure 6C, support this conclusion, illustrating that the vesicle density in the vicinity of the DB determines how long vesicle release can be maintained.

Since data suggest that the DB serves a role in vesicle trafficking and that the three kinetic components of release represent recruitment of vesicles from different morphological pools, a mass action model of vesicle trafficking was developed (Figure 7). The model is based on the hypothesis that release occurred from vesicles on the DB, specifically those vesicles nearest to the plasma membrane, and that this rapidly releasable pool was constantly being refilled from other vesicles attached to the DB. This readily releasable pool was in turn refilled by vesicles surrounding the ribbon, which was refilled by vesicles from a distance. Vesicle pools associated with the DB were assumed to have a maximal capacity and could not be overfilled. Rate constants were assumed to be instantly fully activated at the onset, and fully inactivated at the end, of a stimulus step, simplifying and embedding the presumed time and Ca^{2+}-dependent nature of these processes. The equations describing the equilibrium of each pool are provided in the Experimental Procedures. Vesicle populations associated with the DB (model pools A/B) were constrained by the total number measured experimentally, but the relative distribution between A and B was fit. Optimizing this system of equations for the initial values of vesicle numbers in each pool, and for their associated rate constants, allowed for the fitting of the data presented in Figure 5. The entire response curve was fit, (Figure 5C) and expanded timescales (Figures 7C and 7D) illustrate the ability of the model to reproduce each of the kinetic components of release and to do so with vesicle populations measured morphologically. Rate constants and pool sizes are given in Table 1. The model consistently predicted fewer vesicles in pool A than were counted, suggesting that not all vesicles between the membrane and DB are in the rapidly releasable pool and that perhaps vesicle location is not the sole determinant of pool identity. Other determinants might include the Ca^{2+} gradient across the DB selecting this pool size or some biochemical priming step that may be required prior to release. Values estimated for pool C were higher in low-frequency cells than in high-frequency cells, indicating the need to recruit vesicles from further away and supporting the conclusion that saturation was reached earlier in low-frequency cells than in high-frequency cells due to the lower density of vesicles in the refilling pool.

The model allows for tracking of vesicle populations for each pool (Figure 7B). The rapidly releasable pool declined quickly during depolarization (see arrow) to a relatively steady-state level and maintained this level until all other pools had depleted, suggesting that for the initial 20 ms of stimulation, release was faster than was replenishing, after which the two were comparable. These observations are similar to measurements obtained in frog saccular hair cells, where depolarization depleted the population of vesicles on the DB away from the plasma membrane before it depleted those near the plasma membrane (Lenzi et al., 2002). In fact, it was suggested that vesicles near the DB, but not tethered to it, were depleted first, followed by tethered vesicles on the DB but away from the membrane, followed by tethered vesicles on the DB near the plasma membrane, a scenario reproduced by the model (Figure 7B). The model demonstrates that the difference in the

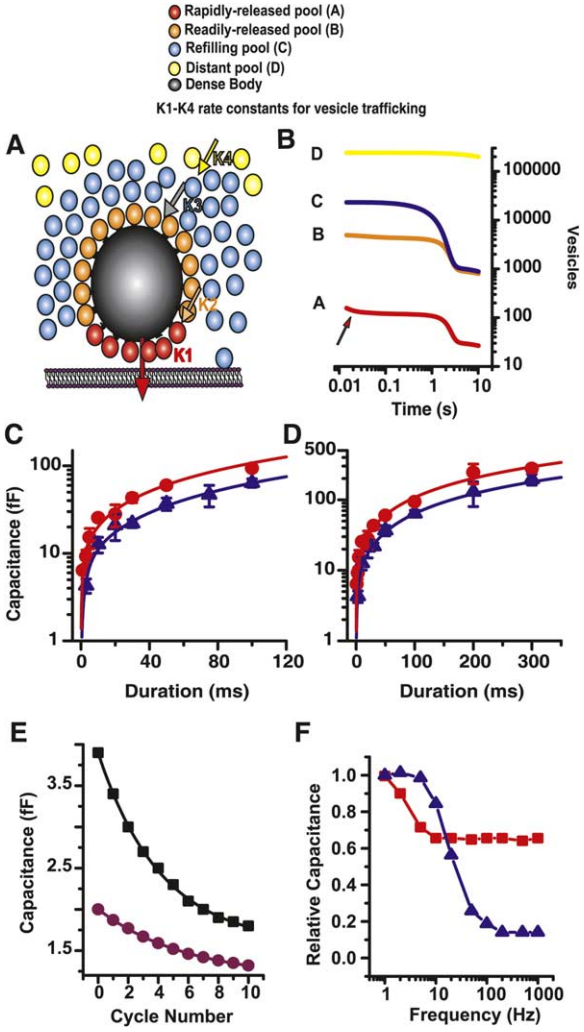

Figure 7. Mass Action Model of Vesicle Trafficking via DB to Membrane Reproduces Both Kinetic and Vesicle Numbers Obtained Empirically

(A) Schematic representation of model features. Four vesicle pools were considered: a rapidly releasable pool of vesicles between the membrane and the DB (pool A, red); a readily releasable pool of the remaining vesicles on the DB (pool B, orange); a refilling pool, comprised of vesicles near, but not on, the DB (pool C, blue); and a distant pool, consisting of cytosolic vesicles (pool D, yellow). K1–K4 represent rate constants for vesicle trafficking.

(B) Change in vesicle populations in each pool during a 10 s depolarization. Vesicle populations are for high-frequency cells, and these values reproduced the model fits in Figures 5C, 7C, and 7D. Arrow indicates rapid reduction in release during the first 20 ms of stimulation.

(C and D) Plotting of data from Figures 5A and 5B, with theoretical fits (solid lines) demonstrating that the model can reproduce each kinetic component of release. Error bars represent the mean ± SD.

(E) Simulation using a 500 Hz sine wave stimulus and plotting the first ten capacitance responses, normalized to the first response using properties from high-frequency cells to reproduce the adaptive rundown described by Furukawa and Matsuura (Furukawa and Matsuura, 1978).

(F) Theoretical responses for high- and low-frequency cells to sinusoidal stimulation using a full-duty cycle. Data were measured at the end of a 5 s stimulus and normalized to a 1 Hz response for both amplitude and time. Simulations predict that synaptic transmission can be maintained during higher- frequency stimulation better in high-frequency cells than in low-frequency cells.

concentration of vesicles near the DB is important in maintaining release during extended depolarizations.

The mass action model was used to address two of the functional consequences of the reported tonotopic differences in synaptic properties. The pioneering work of Furukawa (Furukawa and Matsuura, 1978) demonstrated an adaptive rundown in synaptic transmission of goldfish saccule afferent fibers. Quantal analysis postulated the mechanism of rundown as a change in the number of quanta available for release. Rundown was influenced by stimulus frequency and amplitude. Figure 7B demonstrates that the rapidly released pool of vesicles declined in number over the first 20 ms of stimulation and then plateaued to a baseline level, suggesting that the number of vesicles released per cycle may be reduced. To evaluate the possibility that this initial depletion underlies the mechanism for adaptive rundown, square wave stimulation (500 Hz) was applied to the model. A full and a half-duty cycle were used to alter the period of time over which rate constants were active and release was occurring during each cycle (Figure 7E) to simulate different stimulus amplitudes; a full duty cycle simulated larger-amplitude stimuli. Capacitance plotted against stimulus cycle number reproduced an adaptive rundown due to a decrease in the number of vesicles in the rapidly releasable pool and illustrated that the rundown varies with stimulus amplitude, much as was suggested in goldfish (Furukawa and Matsuura, 1978).

The model was then used to address a basic hypothesis underlying the present work: by increasing the number of synapses, higher-frequency transmission can be obtained. The experiment consisted of simulating responses to different frequencies of stimulation. Steady-state capacitance changes were measured at the end of a 5 s stimulation and normalized to the 1 Hz stimulus response and the total number of cycles. This normalization was necessary to account for the different amounts of time spent releasing ("on-time") at each frequency. For example, 5 cycles of 10 Hz were compared to 1 cycle of 1 Hz. The normalized capacitance change plotted against frequency reveals that high-frequency cells can maintain release at higher frequencies better than can low-frequency cells and, surprisingly, that low- frequency cells respond better at low frequencies. That the model is capable of these predictions is remarkable, as no Ca^{2+} dependence was included for any step of release or trafficking, and it suggests that vesicle trafficking and release and the morphological limitations imposed by the structures are of fundamental importance in shaping synaptic transmission.

Discussion

Results from this work suggest that high-frequency synaptic transmission is promoted by increasing the number of synapses and the number of vesicles near the DB and by decreasing the Ca^{2+} load per synapse in comparison with low-frequency synapses. These changes enable high-frequency cells to maintain release for longer periods of time while releasing at slower rates per synapse than low-frequency cells. This mechanism

Table 1. Values Obtained from Fitting the Capacitance Data in Figures 4 and 5 with the Mass Action Model

Model Parameter	Low-Frequency Model	Low-Frequency Measured	High-Frequency Model	High-Frequency Measured
Na	103 (6)	28 ± 10 (10)	555 (9)	32 ± 9 (10)
Nb	1139 (63)	69 ± 11 (7)	5085 (85)	94 ± 21 (11)
Nc	37548 (1.47 μm)	1416 ± 220 ves/μm^3	23114 (0.16 μm)	2354 ± 459 ves/μm^3
Nd	1352	595 ± 132 ves/μm^3	242071	475 ± 98 ves/μm^3
Ka	501 s^{-1}		150 s^{-1}	
Kb	17.4 s^{-1}		5.26 s^{-1}	
Kc	1.59 s^{-1}		5.34 s^{-1}	
Kd	1.32 s^{-1}		0.02 s^{-1}	

N_x represents the vesicles in each pool a–d, using 50 aF as the capacitance of a single vesicle. K represents the rate constant for trafficking of vesicles between morphologically defined pools. Na + Nb was constrained to be equivalent to the number of vesicles per DB, obtained from morphological counts. Values in parentheses for the model are normalized to the number of synapses, except for Nc, which is the distance from the DB that encompasses the estimated number of vesicles. Measured values are vesicle counts from the EM analysis normalized to the number of synapses; data in parentheses represent the numbers of samples.

differs from mechanisms found in species that hear at higher frequencies (≥10 kHz), such as birds and mammals. In bird, the number of synapses is relatively constant across cells of different frequencies (Martinez-Dunst et al., 1997), and mammals tend to have a single synapse per afferent fiber and multiple fibers (Liberman et al., 1990). In addition, the I_{Ca} in both bird and mammal is smaller than that in turtle, despite their higher-frequency hearing. These differences may suggest several limitations of the mechanism used in turtle. As the fastest release rate measured was 50,000 ves/s, the ability to release at high rates would not be rate limiting; however, the limitation may come from postsynaptic summation and integration. A loss of postsynaptic temporal resolution may require fewer synapses to be used at higher frequencies. The fastest release rate measured for a single site was 1389 ves/s/DB, suggesting that the basic mechanisms of release and refilling may be comparable among species and between ribbon synapses. However, on a cycle-by-cycle basis, the Ca^{2+} load needed to promote release, and refilling may limit the frequency response as Ca^{2+} clearance may become rate-limiting at higher frequencies. One caveat to this discussion is the assumption that all morphologically identified synapses are functional: it is possible that some percentage of synapses are silent.

An unexpected finding was that release rates normalized to the number of release sites were faster in low-frequency cells than in high-frequency cells. The difference in rates might reflect the higher Ca^{2+} load per release site in low-frequency cells. A reduced release rate may prevent postsynaptic receptor saturation. Thus, in high-frequency cells overall higher frequencies of release are obtained primarily as a result of a greater number of synapses. These are then translated synaptically with greater fidelity by limiting postsynaptic saturation by reducing the release rate per synapse (Taschenberger et al., 2002). A reduction in release per DB will slow depletion at any given site, as is apparent from the multipulse stimulation data of Figure 6. An additional consequence of reduced Ca^{2+} load per release site is the reduced requirement for Ca^{2+} clearance, promoting operation at higher frequencies. Thus, hypotheses regarding species differences also hold true for different frequency positions within a given end organ.

Ca^{2+} dependence of release was linear over a wide range of Ca^{2+} loads and capacitance values (Figure 4C). The sensitivity, 0.90 ± 0.03 fF/pC, was comparable to that reported for the mature mouse inner hair cell (0.7 fF/pC), again supporting the conclusion that basic mechanisms of release are conserved (Johnson et al., 2005). Functionally, the linearity allows information from small graded receptor potentials to be transferred in a graded manner across the synapse, as in photoreceptors (Thoreson et al., 2004). One consequence of the shallow slope of the Ca^{2+}-dependence plot is that higher Ca^{2+} levels are required for release and, thus, release may be slowed in comparison to that for traditional synapses when normalized to absolute Ca^{2+} levels. This supports the hypothesis that linearity over such a broad capacitance range implies that the rate-limiting step may be Ca^{2+}-driven vesicle fusion.

The three kinetic components of release reported here show more overlap in time compared to the kinetic components reported in other ribbon synapses (Eisen et al., 2004; Mennerick and Matthews, 1996; Johnson et al., 2005). One explanation might be the size of the DB (or synaptic ribbons) in relation to the Ca^{2+} gradients produced by clustered Ca^{2+} channels. As shown here, auditory hair cells have small DBs but large I_{Ca} compared to other ribbon type synapses where DBs are larger and I_{Ca} is smaller. It is possible that release and refilling kinetics are dictated by spatial Ca^{2+} gradients across DBs and that the apparent overlap in kinetics reported here is a manifestation of the smaller DBs and the larger I_{Ca}. Regardless of mechanisms, the overlap in kinetics suggests that refilling rates are comparable or faster than release rates.

Morphological, electrophysiological, and theoretical data presented are consistent with the hypothesis that the DB acts to prevent depletion of releasable vesicles by navigating large numbers of cytosolic vesicles to release sites in short periods of time. This idea is not new and has been invoked for both auditory and visual system cells containing synaptic ribbons (Lagnado, 2003; Parsons and Sterling, 2003; von Gersdorff and Matthews, 1999). One problem with this theory is that vesicle movements are extremely fast. For the release rates identified here, where vesicles on the DB are proposed to be released, a vesicle needs to travel at a rate of 300 nm/s to traverse from the farthest point on the DB to the release site, a value faster than that in either

kinesin or myosin motors. One partial explanation may be that vesicles can attach to the DB at any point and need not travel the entire length of the DB during rapid stimulation.

The present work suggests that the DB plays an important role in vesicle trafficking and that the basic functions of the DB may be conserved across species and sensory modalities. A simple model of vesicle trafficking can reproduce the electrophysiological and morphological data obtained, suggesting that trafficking is the major determinant of release properties. In turtle, synaptic specializations include an increase in the number of release sites and in the density of vesicles near the DB and a decrease in Ca^{2+} load per synapse in high- compared with low-frequency cells. The model of vesicle trafficking supports the long-standing hypothesis that adaptive rundown is generated by a decrease in available vesicles for release and also demonstrates that measured differences in release result in synapses operating most efficiently near the hair cell's best frequency.

Experimental Procedures

Tissue Preparation

The turtle auditory papilla is a well-described model for investigating auditory physiology (Crawford and Fettiplace, 1985; Ricci and Fettiplace, 1997). Red-eared sliders (*Trachemys scripta elegans*), with a carapace length of 3 in to 5 in were decapitated, and the inner ear organs were removed using procedures approved by the ACUC committee at LSU Health Sciences Center and standards established by NIH guidelines. The inner ear organs were placed into external solution containing 125 mM NaCl, 0.5 mM KCl, 2.8 mM $CaCl_2$, 2.2 mM $MgCl_2$, 2 mM pyruvate, 2 mM creatine, 2 mM lactate, 2 mM ascorbate, 6 mM glucose, and 10 mM N-(2-Hydroxyethyl) piperazine-N'-(2-ethanesulfonic acid) (HEPES) at a pH of 7.6 and with a final osmolality of 275 mOsm/kg. The tissue was pinned to the bottom of a dish with the auditory papilla facing upward and incubated in a normal Ca^{2+} solution for 25 min, after which the tectorial membrane was removed. The tissue was trimmed, placed into the recording chamber, and perfused at 1–3 ml/h. Mechanically gated transduction currents were eliminated by spraying a 1 mM BAPTA solution onto the hair bundles prior to recording (Ricci et al., 2003). For imaging experiments, the brain was removed from the turtle half-head and Alexa 488 crystals (Molecular Probes) were placed onto the stump of the 8th nerve. Timing of the dye application was critical in that too great a delay resulted in failure of dye uptake by the nerve endings, presumably due to resealing of the nerve stump.

Two-Photon Imaging

A custom designed two-photon system was used, based on that of Majewska et al. (Majewska et al., 2000) and Nikolenko et al. (Nikolenko et al., 2003), who modified the Olympus Fluoview confocal system. The galvanometers from the Olympus scanhead were used to direct the Mira 900 pulsed laser onto the tissue. An excitation wavelength of 840 nm with a half-power width of ~9 nm was used. An external Hamamatsu photomultiplier tube (PMT) was attached to the epifluorescent path of the Olympus BX50 microscope with a BG39 (Chroma Technologies) bandpass (520 nm) filter and placed in front of the PMT. The output was fed into the Olympus Fluoview system to allow PMT voltage and sampling as well as digital gain and offset to be controlled by the Fluoview software. A dichroic mirror (660 nm long pass; 660 Dcxxr; Omega Opticals) was used to direct the emitted light to the PMT.

Electron Microscopy

Because diurnal variations have been ascribed to DBs and could confound morphologic evaluations, all animals were housed on a strict 12 hr:12 hr light:dark cycle, and all tissues were fixed at approximately the same point in this light cycle. (Adly et al., 1999; Balkema et al., 2001). High- and low-frequency DBs from the same tissue were evaluated as internal controls. Tissue was fixed with a solution containing 2.5% glutaraldehyde, 1% paraformaldehyde, 0.1M Cacodylate buffer, and 2 mM $CaCl_2$ (pH, adjusted to 7.4) (Hackney et al., 1993). Turtles (n = 6) were decapitated, and the head was bisected sagitally. Fixative was injected directly into the perilymphatic space, and each half-head placed into fixative overnight and refrigerated. The tissue was then dissected out in a 1:10 dilution of the fixative. After postfixation for 1 hr with 1% osmium tetroxide in the same buffer, samples were dehydrated through an ethanol series and embedded in Spurr's resin (Hackney et al., 1993). To obtain data from different frequency locations, the resin-embedded samples were trimmed to obtain longitudinal sections of the basilar papilla.

To determine the number of synapses per hair cell, 300 nm thick serial sections were cut and mounted onto a modified JEOL bulk specimen holder with a 10 × 2 mm slot drilled into it, covered with a pioloform or formvar film. They were examined unstained in a JEOL 100CX TEM. Typically, 60 sections were needed to pass through an entire cell. Only cells in which the beginning and end points could be clearly delineated were included. Low-power images identified the hair cell edge, ensuring that the entire hair cell was included, while higher magnifications were used to identify synapses.

For determination of synaptic vesicle numbers and distributions, 40 nm ultrathin serial sections were mounted onto standard formvar- or pioloform-coated 1 × 2 mm slot grids, stained with uranyl acetate and lead citrate, and examined in a JEOL1230 or 100CX TEM. Images of synaptic DB and other regions of the hair cells were obtained using a Megaview III digital camera at selected proportional distances along the papilla from the apical end and analyzed using analySIS software (see Figure 2 for an example of a complete series through a DB). Section thickness was assessed by using the interference color of the section floating on water, with gray/silver indicating ~40 nm and blue/green representing ~300 nm.

Electrophysiology

Capacitance measurements were made in voltage-clamp with a lock-in amplifier (Cairn) (Johnson et al., 2002), using methods described by Neher and Marty (Neher and Marty, 1982). A ±40 mV, 1.5 kHz sinusoidal stimulation was imposed onto the holding potential. The sine wave was blanked during depolarization and then resumed immediately upon repolarization to capture precapacitance and postcapacitance measurements. Capacitance data were amplified 10–50× and filtered at 100 Hz offline. The internal solution contained (in mM) 110 mM CsCl, 5 mM MgATP, 5 mM creatine phosphate, 1 mM ethylene glycol-bis (β-amino ethyl ether)-N,N,N',N'-tetraacetic acid (EGTA), 10 mM HEPES, 2 mM ascorbate (pH, 7.2). Cells were excluded if series resistance or leak conductance varied by more than 25% during the recording. All experiments were performed between 19° and 22°C. Apamin at 100 nM was included for all experiments to block the SK potassium conductance (Tucker and Fettiplace, 1996). All data were sampled at 3–20 kHz with a CED AD converter and controlled through a computer with Signal software (CED). Protocols that varied the duration of the depolarization were randomized for durations up to 1 s; longer durations were performed as a final stimulation or on separate cells, as recovery was often limited. Cells were allowed to equilibrate upon reaching whole-cell mode for 15 min (Schnee and Ricci, 2003) and then to recover between stimuli for up to 10 min, depending on stimulus duration.

Data Analysis

Cells were included for analysis of capacitance data according to the size of the I_{Ca} and the capacitance change elicited by a 100 ms depolarization to –20mV. High-frequency cells required I_{Ca} >600 pA (Schnee and Ricci, 2003) and a capacitance response >45 fF, while low-frequency cells required I_{Ca} >300 pA and capacitance changes >30 fF. Cells were also required to have stable series resistances <10 MΩ (uncompensated) and leak currents < 50 pA at –80mV. Unless otherwise stated, data are presented as the mean ± stan-

dard deviation. Statistical comparisons were performed using a two-tailed Student's t test.

Vesicle Measurements

All measurements were made using Image J software from NIH. Vesicles were chosen for diameter measurements only if a clear line of membrane could be observed, indicating a membrane orthogonal to the section plane. This should only occur when the vesicle has reached its maximum diameter. Measurements were confirmed using stereo pairs and also by comparing measurements from tissues sectioned at varying thicknesses (see Results). As the vesicles often did not appear spherical, their diameter was estimated by measuring the area of the vesicle profile and calculating the diameter by assuming a circle of equivalent area. Vesicles were counted as being associated with the DB if they lay within 30 nm of it (Lenzi et al., 1999). Maximal densities of vesicles were estimated with the method described in Lenzi et al. (Lenzi et al., 1999), using the smallest hexagon into which the circle of 42 nm could fit and then calculating the number of hexagons that could be fit into its area. The surface area used for the DB was calculated using the radius of a fitted sphere of the DB plus the vesicle radius plus a tether length taken from Lenzi et al. (Lenzi et al., 1999).

Modeling

A model is presented that incorporates vesicles moving from one pool to another and then being released. A mass action kinetic process was used, and activation of the process was assumed to happen in a stepwise manner. That is, rate constants were assumed to be instantly fully activated at the onset, and fully inactivated at the end, of a stimulus step. For multiple steps, a full-duty cycle implied that the time activated was equal to the time inactivated during a cycle; a half-duty cycle implied that the time activated was half of the time inactivated during a cycle. The model is schematically represented in Figure 7A. The equations defining the equilibration of vesicles include:

$$dF/dt = k_1 * A(t) \quad (1)$$

$$dA/dt = k_2 * B(t) * (A_t - A(t))/A_t - k_1 * A(t) \quad (2)$$

$$dB/dt = k_3 * C(t) * ((B_t - B(t))/B_t - k_2 * B(t) * (A_t - A(t)/A_t) \quad (3)$$

$$dC/dt = k_4 * D(t) - k_3 * C(t) * (B_t - B(t))B_t \quad (4)$$

$$dD/dt = -k_4 * D(t) \quad (5)$$

F(t) is the number of vesicles inserted into the membrane and is related to time-dependent capacitance changes by the conversion factor of 50×10^{-3} fF/vesicle. A(t)–D(t) are the time-dependent number of vesicles in each pool at any given time for rapidly releasable, readily releasable, refilling and distant pools. A_t and B_t are the maximal number of vesicles in these pools, which are equivalent to the initial vesicle numbers. K1–K4 are rate constants. This system of equations was solved using a fourth-order Runge-Kutta method. The number of initial vesicles in each pool and the rate constants were optimized to fit the experimental capacitance data from either high- or low-frequency cells by a genetic algorithm (Taylor and Enoka, 2004). The genetic algorithm provides a globally unique solution for the ranges of parameters sampled (Youngs, 2002). Vesicular pool sizes were varied from 1 to 10^7; rate constants were varied from 10^{-3} to 10^3. A mutation rate of 0.2 and a crossover rate of 0.6 were used. Solutions converged with a stable error over 100 generations after 500–1000 generations.

Acknowledgments

Our thanks to K.J. Rennie, R. Fettiplace, and J. Magee for useful discussions. This work was supported by R01-DC03896 to A.J.R.

Received: December 22, 2004
Revised: May 5, 2005
Accepted: June 1, 2005
Published: July 20, 2005

References

Adly, M.A., Spiwoks-Becker, I., and Vollrath, L. (1999). Ultrastructural changes of photoreceptor synaptic ribbons in relation to time of day and illumination. Invest. Ophthalmol. Vis. Sci. *40*, 2165–2172.

Balkema, G.W., Cusick, K., and Nguyen, T.H. (2001). Diurnal variation in synaptic ribbon length and visual threshold. Vis. Neurosci. *18*, 789–797.

Crawford, A.C., and Fettiplace, R. (1980). The frequency selectivity of auditory nerve fibres and hair cells in the cochlea of the turtle. J. Physiol. *306*, 79–125.

Crawford, A.C., and Fettiplace, R. (1985). The mechanical properties of ciliary bundles of turtle cochlear hair cells. J. Physiol. *364*, 359–379.

Eisen, M.D., Spassova, M., and Parsons, T.D. (2004). Large releasable pool of synaptic vesicles in chick cochlear hair cells. J. Neurophysiol. *91*, 2422–2428.

Fettiplace, R., and Fuchs, P.A. (1999). Mechanisms of hair cell tuning. Annu. Rev. Physiol. *61*, 809–834.

Furukawa, T., and Matsuura, S. (1978). Adaptive rundown of excitatory post-synaptic potentials at synapses between hair cells and eight nerve fibres in the goldfish. J. Physiol. *276*, 193–209.

Furukawa, T., Hayashida, Y., and Matsuura, S. (1978). Quantal analysis of the size of excitatory post-synaptic potentials at synapses between hair cells and afferent nerve fibres in goldfish. J. Physiol. *276*, 211–226.

Gleisner, L., Flock, A., and Wersall, J. (1973). The ultrastructure of the afferent synapse on hair cells in the frog labyrinth. Acta Otolaryngol. *76*, 199–207.

Gomis, A., Burrone, J., and Lagnado, L. (1999). Two actions of calcium regulate the supply of releasable vesicles at the ribbon synapse of retinal bipolar cells. J. Neurosci. *19*, 6309–6317.

Gray, E.G., and Pease, H.L. (1971). On understanding the organisation of the retinal receptor synapses. Brain Res. *35*, 1–15.

Hackney, C.M., Fettiplace, R., and Furness, D.N. (1993). The functional morphology of stereociliary bundles on turtle cochlear hair cells. Hear. Res. *69*, 163–175.

Hama, K., and Saito, K. (1977). Fine structure of the afferent synapse of the hair cells in the saccular macula of the goldfish, with special reference to the anastomosing tubules. J. Neurocytol. *6*, 361–373.

Holt, M., Cooke, A., Neef, A., and Lagnado, L. (2004). High mobility of vesicles supports continuous exocytosis at a ribbon synapse. Curr. Biol. *14*, 173–183.

Issa, N.P., and Hudspeth, A.J. (1994). Clustering of Ca2+ channels and Ca(2+)-activated K+ channels at fluorescently labeled presynaptic active zones of hair cells. Proc. Natl. Acad. Sci. USA *91*, 7578–7582.

Jacobs, R.A., and Hudspeth, A.J. (1990). Ultrastructural correlates of mechanoelectrical transduction in hair cells of the bullfrog's internal ear. Cold Spring Harb. Symp. Quant. Biol. *55*, 547–561.

Johnson, S.L., Thomas, M.V., and Kros, C.J. (2002). Membrane capacitance measurement using patch clamp with integrated self-balancing lock-in amplifier. Pflugers Arch. *443*, 653–663.

Johnson, S.L., Marcotti, W., and Kros, C.J. (2005). Increase in efficiency and reduction in Ca2+ dependence of exocytosis during development of mouse inner hair cells. J. Physiol. *563*, 177–191.

Kollmar, R., Montgomery, L.G., Fak, J., Henry, L.J., and Hudspeth, A.J. (1997). Predominance of the alpha1D subunit in L-type voltage-gated Ca2+ channels of hair cells in the chicken's cochlea. Proc. Natl. Acad. Sci. USA *94*, 14883–14888.

Lagnado, L. (2003). Ribbon synapses. Curr. Biol. *13*, R631.

Lagnado, L., Gomis, A., and Job, C. (1996). Continuous vesicle cy-

cling in the synaptic terminal of retinal bipolar cells. Neuron *17*, 957–967.

Lenzi, D., Runyeon, J.W., Crum, J., Ellisman, M.H., and Roberts, W.M. (1999). Synaptic vesicle populations in saccular hair cells reconstructed by electron tomography. J. Neurosci. *19*, 119–132.

Lenzi, D., Crum, J., Ellisman, M.H., and Roberts, W.M. (2002). Depolarization redistributes synaptic membrane and creates a gradient of vesicles on the synaptic body at a ribbon synapse. Neuron *36*, 649–659.

Liberman, M.C., Dodds, L.W., and Pierce, S. (1990). Afferent and efferent innervation of the cat cochlea: quantitative analysis with light and electron microscopy. J. Comp. Neurol. *301*, 443–460.

Majewska, A., Yiu, G., and Yuste, R. (2000). A custom-made two-photon microscope and deconvolution system. Pflugers Arch. *441*, 398–408.

Martinez-Dunst, C., Michaels, R.L., and Fuchs, P.A. (1997). Release sites and calcium channels in hair cells of the chick's cochlea. J. Neurosci. *17*, 9133–9144.

Mennerick, S., and Matthews, G. (1996). Ultrafast exocytosis elicited by calcium current in synaptic terminals of retinal bipolar neurons. Neuron *17*, 1241–1249.

Moser, T., and Beutner, D. (2000). Kinetics of exocytosis and endocytosis at the cochlear inner hair cell afferent synapse of the mouse. Proc. Natl. Acad. Sci. USA *97*, 883–888.

Neher, E., and Marty, A. (1982). Discrete changes of cell membrane capacitance observed under conditions of enhanced secretion in bovine adrenal chromaffin cells. Proc. Natl. Acad. Sci. USA *79*, 6712–6716.

Neves, G., and Lagnado, L. (1999). The kinetics of exocytosis and endocytosis in the synaptic terminal of goldfish retinal bipolar cells. J. Physiol. *515*, 181–202.

Nikolenko, V., Nemet, B., and Yuste, R. (2003). A two-photon and second-harmonic microscope. Methods *30*, 3–15.

Parsons, T.D., and Sterling, P. (2003). Synaptic ribbon. Conveyor belt or safety belt? Neuron *37*, 379–382.

Parsons, T.D., Lenzi, D., Almers, W., and Roberts, W.M. (1994). Calcium-triggered exocytosis and endocytosis in an isolated presynaptic cell: capacitance measurements in saccular hair cells. Neuron *13*, 875–883.

Ricci, A.J., and Fettiplace, R. (1997). The effects of calcium buffering and cyclic AMP on mechano-electrical transduction in turtle auditory hair cells. J. Physiol. *501*, 111–124.

Ricci, A.J., Gray-Keller, M., and Fettiplace, R. (2000). Tonotopic variations of calcium signaling in turtle auditory hair cells. J. Physiol. *524*, 423–436.

Ricci, A.J., Crawford, A.C., and Fettiplace, R. (2003). Tonotopic variation in the conductance of the hair cell mechanotransducer channel. Neuron *40*, 983–990.

Roberts, W.M., Jacobs, R.A., and Hudspeth, A.J. (1990). Colocalization of ion channels involved in frequency selectivity and synaptic transmission at presynaptic active zones of hair cells. J. Neurosci. *10*, 3664–3684.

Rouze, N.C., and Schwartz, E.A. (1998). Continuous and transient vesicle cycling at a ribbon synapse. J. Neurosci. *18*, 8614–8624.

Schnee, M.E., and Ricci, A.J. (2003). Biophysical and pharmacological characterization of voltage-gated calcium currents in turtle auditory hair cells. J. Physiol. *549*, 697–717.

Sneary, M.G. (1988). Auditory receptor of the red-eared turtle: II. Afferent and efferent synapses and innervation patterns. J. Comp. Neurol. *276*, 588–606.

Taschenberger, H., Leao, R.M., Rowland, K.C., Spirou, G.A., and von Gersdorff, H. (2002). Optimizing synaptic architecture and efficiency for high-frequency transmission. Neuron *36*, 1127–1143.

Taylor, A.M., and Enoka, R.M. (2004). Optimization of input patterns and neuronal properties to evoke motor neuron synchronization. J. Comput. Neurosci. *16*, 139–157.

Thoreson, W.B., Rabl, K., Townes-Anderson, E., and Heidelberger, R. (2004). A highly Ca2+-sensitive pool of vesicles contributes to linearity at the rod photoreceptor ribbon synapse. Neuron *42*, 595–605.

Tucker, T., and Fettiplace, R. (1995). Confocal imaging of calcium microdomains and calcium extrusion in turtle hair cells. Neuron *15*, 1323–1335.

Tucker, T.R., and Fettiplace, R. (1996). Monitoring calcium in turtle hair cells with a calcium-activated potassium channel. J. Physiol. *494*, 613–626.

Usukura, J., and Yamada, E. (1987). Ultrastructure of the synaptic ribbons in photoreceptor cells of Rana catesbeiana revealed by freeze-etching and freeze-substitution. Cell Tissue Res. *247*, 483–488.

von Gersdorff, H., and Matthews, G. (1994). Dynamics of synaptic vesicle fusion and membrane retrieval in synaptic terminals. Nature *367*, 735–739.

von Gersdorff, H., and Matthews, G. (1997). Depletion and replenishment of vesicle pools at a ribbon-type synaptic terminal. J. Neurosci. *17*, 1919–1927.

von Gersdorff, H., and Matthews, G. (1999). Electrophysiology of synaptic vesicle cycling. Annu. Rev. Physiol. *61*, 725–752.

von Gersdorff, H., Vardi, E., Matthews, G., and Sterling, P. (1996). Evidence that vesicles on the synaptic ribbon of retinal bipolar neurons can be rapidly released. Neuron *16*, 1221–1227.

Youngs, I.J. (2002). Exploring the universal nature of electrical percolation exponents by genetic algorithm fitting with general effective medium theory. J. Phys. D Appl. Phys. *35*, 3127–3137.

Zenisek, D., Davila, V., Wan, L., and Almers, W. (2003). Imaging calcium entry sites and ribbon structures in two presynaptic cells. J. Neurosci. *23*, 2538–2548.